

A physical model for the continuum variability and QPO in accreting black holes

Adam Ingram^{1*} & Chris Done¹

¹Department of Physics, University of Durham, South Road, Durham DH1 3LE, UK

Submitted to MNRAS

ABSTRACT

The power spectra of black hole binaries have been well studied for decades, giving a very detailed phenomenological picture of the variability properties and their correlation with the energy spectrum (spectral state) of the source. Here we take the truncated disc/hot inner flow picture which can describe the spectral changes, and show that propagating mass accretion rate fluctuations in the hot flow can match the broad band power spectral properties seen in black hole binaries, i.e. give approximately band limited noise between a low and high frequency break. The low frequency break marks the viscous timescale at the outer edge of the hot inner flow, which is the inner edge of the truncated disc. The fluctuations in mass accretion rate propagate towards the central object in a finite time meaning the high frequency break is more complex than simply the viscous timescale at the inner edge of the hot flow because fluctuations on timescales shorter than the propagation time are incoherent. The model also predicts the Lense-Thirring precession timescale of the hot flow, as this is set by the combination of inner and outer radius of the flow, together with its surface density which is self consistently calculated from the propagating fluctuations. We show that this naturally gives the observed relation between the low frequency break and QPO frequency as the outer radius of the flow moves inwards, and that this model predicts many of the observed QPO properties such as correlation of coherence with frequency, and of the recently discovered correlation of frequency with flux on short timescales.

We fit this total model of the variability to a sequence of 5 observed power spectra from the bright black hole binary XTE J1550-564 as the source transitioned from a low/hard to very high state. This is the first time that a power spectrum from a black hole binary has been fit with a physical model for the variability. The data are well fit if the inner radius of the flow remains constant, while the outer radius sweeps inwards from $\sim 75 - 12R_g$. This range of radii is the same range as required by models of the energy spectral evolution, giving the first self consistent description of the evolution of both the spectrum and variability of BHB.

Key words: X-rays: binaries – accretion, accretion discs

1 INTRODUCTION

Emission observed from Black Hole Binaries (BHBs) is variable on both long and short timescales. On the longest timescales, changes in mass accretion rate drive changes in spectral state. At the lowest luminosities, the system is typically seen in the low/hard state, where the spectrum is dominated by a hard (photon index $\Gamma < 2$) power law tail, peaking at 100 keV. As the source brightens, there is an increasing contribution from the disc at low energies and the tail softens towards $\Gamma \sim 2$ (intermediate state). The tail can then either remain strong as the source flux increases, giving the very high state ($\Gamma \sim 2.5$) or it can carry only a very small fraction of the

luminosity, giving the high/soft state ($\Gamma \sim 2.2$) (e.g. see reviews by Remillard & McClintock 2006; Done, Gierlinski & Kubota 2007, hereafter DGK07).

Much of this long term spectral evolution can be successfully described by the truncated disc model (DGK07). Here, the assumption is that the cool, geometrically thin, optically thick disc is truncated at some radius, r_o , which is much larger than the last stable orbit, r_{lso} at the lowest luminosities. The inner accretion flow extends from r_o to an innermost radius, r_i , forming some sort of hot, geometrically thick, optically thin (optical depth $\tau \sim 1.5$) flow, similar to an Advection Dominated Accretion Flow (ADAF, Narayan & Yi 1995). Decreasing the truncation radius of the thin disc with increasing luminosity (and therefore average mass accretion rate) leads to a stronger disc component and greater illumina-

* E-mail:a.r.ingram@durham.ac.uk

tion of the hot flow by the cool disc photons and hence to a softer Comptonised tail. This spectral evolution has a natural end when $r_o \sim r_{iso}$, marking the transition to the disc dominated soft states seen at higher luminosities.

There is also rapid variability on timescales of 100-0.1s which is almost exclusively linked to the Comptonised tail (e.g. Churazov et al 2001). This is as expected as the disc emission can only vary on a viscous timescale of $t_{visc} = 4.5 \times 10^{-3} \alpha^{-1} (h/r)^{-2} (R/6R_g)^{3/2} (M/10M_\odot)$ s i.e. 500 s at the last stable orbit for fiducial thin disc parameters of $h/r \sim 0.01$ and $\alpha = 0.1$.

A power spectral analysis of the rapid variability shows that it is generally composed of a broadband noise continuum, with a low frequency quasi-periodic oscillation (LF QPO) superimposed on this. The broadband noise can be very roughly characterized as a twice broken power law, with $fP_f \propto f$ at the lowest frequencies, breaking to $fP_f \propto f^0$ above the low frequency break f_b , and then breaking again to $fP_f \propto f^{-1}$ above a high frequency break at f_h . The low frequency break is tightly correlated with the spectral state of the source, with $f_b \sim 0.01$ Hz for the dimmest low/hard states, and increasing to ~ 1 Hz as the source softens through the bright low/hard states into the intermediate state. The LF QPO properties are also tightly correlated with this power spectral and energy spectral evolution, with QPO frequency $f_{QPO} \sim 10f_b$ increasing from 0.1-10 Hz, as the coherence, power and harmonic content of this feature also increase (e.g. van der Klis et al 2004). Again, this can be interpreted qualitatively in the truncated disc picture if the low frequency break and QPO are somehow associated with the truncation radius. As the disc extends further inwards, the spectrum softens, and all frequencies associated with this radius increase (e.g. DGK07).

However, to go beyond this into a quantitative description requires a specific model for both the broadband noise and QPO. This is problematic, despite both having been known for many decades (e.g. van der Klis 1989). There are multiple potential models for the LF QPO in the literature which fall into 2 main categories: those associated with a geometrical misalignment of the accretion flow and black hole spin (Stella & Vietri 1998; Fragile, Mathews & Wilson 2001; Schnittman 2005; Schnittman et al 2006; Ingram, Done & Fragile 2009, hereafter IDF09), and those associated with wave modes of the accretion flow (Wagoner et al 2001; Titarchuk & Oscherovich 1999; Cabanac et al 2008). Most of these concentrate on matching the QPO frequency, but the spectrum of the QPO gives additional constraints. This is similar to that of the spectrum of the broadband variability, showing that they both arise predominantly from the Comptonising region rather than the disc (e.g Gilfanov et al 2003; Sobolewska & Zycki 2006), favoring models in which the modulation arises directly from the Comptonised emission e.g. IDF09, where the QPO is set by Lense-Thirring (vertical) precession of the entire hot inner flow interior to the disc truncation radius at r_o , or by a mode of the hot inner flow (Cabanac et al 2008).

The physical origin for the viscosity of the flow is the Magneto-Rotational Instability (MRI: Balbus & Hawley 1991). This is inherently variable, with large fluctuations in all quantities, both spatially and temporally (Krolik & Hawley 2002), making it a natural origin for the broad band noise (Noble & Krolik 2009; Ingram & Done 2010; Dexter & Fragile 2011). However, these fluctuations also effectively shred any coherent wave modes in the flow (see e.g. Reynolds & Miller 2009; Henisey et al 2009). This effectively rules out trapped wave propagation as the origin of the LF QPO, leaving Lense-Thirring precession as the most likely candidate. Precession of the entire hot flow from r_o to r_i can match the

observed LF QPO frequency in both BHBs (IDF09) and neutron stars (NS; Ingram & Done 2010), and provides a clear mechanism to match the spectrum as this is a modulation of the Comptonising region.

Thus the entire power spectrum can be explained by MRI fluctuations in a hot flow, which is also precessing around the black hole. However, the power spectrum does not represent all the information contained in the variability, as it uses only Fourier amplitudes, not phases. This is important as the light curves contain additional correlations which give a linear rms-flux relation (Uttley & McHardy 2001). Short segments of a longer light curve have a mean, I , and variance, σ^2 , which are related such that $I \propto \sigma$ (after binning: Uttley & McHardy 2001). This is equivalent to the flux on these timescales having a log-normal distribution (Negoro et al 2000), and rules out simple models of the variability where the light curve is made from adding together multiple, uncorrelated events (Uttley & McHardy 2001; see also DGK07). Instead, this can be produced if the light curve is made from a multiplicative process, rather than an additive one. Again, the MRI in the hot flow gives a physical interpretation to this. The MRI at large radii produces intrinsic fluctuations in the density of the flow. These fluctuations propagate down to smaller radii on a viscous timescale, so all higher frequency fluctuations are smoothed out. These smoothed and lagged fluctuations in mass accretion rate modulate the MRI fluctuations produced by the next radius, and so on, down to the smallest radii in the flow (Lubarski 1997: hereafter L97). This naturally produces a light curve which has an rms-flux relation/log-normal flux distribution (Kotov et al 2001: hereafter K01; Arevalo & Uttley 2006: hereafter AU06; also see Misra & Zdziarski 2008).

Here we use these ideas to build a model for the entire power spectrum, where the broadband noise arises from propagation of MRI fluctuations through the hot flow from r_o to r_i and the LF QPO arises from Lense-Thirring precession of the same hot flow. We fit this model to a sequence of power spectra of XTE J1550-564 observed during a transition from low/hard to intermediate state, and show that these give a good quantitative fit for r_o moving from $\sim 75 - 10R_g$, as also required to explain the sequence in energy spectra during this transition. This gives very strong support to the underlying truncated disc geometry, and for Lense-Thirring precession as the physical origin for the LF QPO.

2 THE SIMPLIFIED MODEL

We first introduce the simplified toy model considered in IDF09 and Ingram & Done (2010), whereby the low frequency break, f_b , occurs at the viscous frequency of the truncation radius and the QPO frequency, f_{QPO} , is the precession frequency of the flow. Using the Shakura Sunyaev (1973) viscosity prescription, $f_b = f_{visc}(r_o) = \alpha(h/r)^2 f_k(r_o) = -v_r(r_o)/R_o$ where α is the viscosity parameter, h/r the flow semi-thickness, f_k the Keplerian frequency and v_r is the infall velocity. The Lense-Thirring precession frequency is then a weighted average of the point particle precession frequency at each radius in the hot flow, so

$$f_{prec} = f_{QPO} = \frac{\int_{r_i}^{r_o} f_{LT} f_k \Sigma r^3 dr}{\int_{r_i}^{r_o} f_k \Sigma r^3 dr} \quad (1)$$

(Liu & Melia 2002) where r_i is the innermost point of the flow (i.e. the surface density is negligible interior to this), Σ is the surface density and

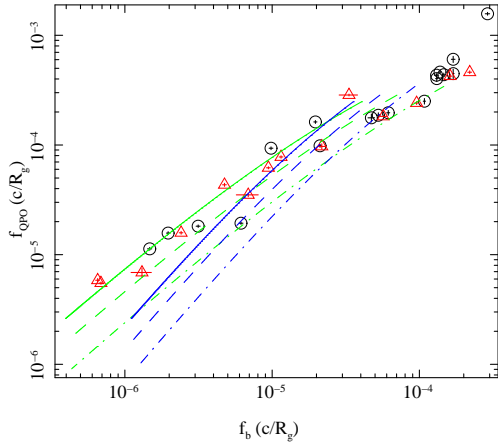


Figure 1. The QPO-break relation plotted in dimensions of c/R_g for a fiducial mass of 10 and $1.4M_\odot$ for black holes (black circles) and neutron stars (red triangles) respectively. The fact that these frequencies lie on the same relationship for the two objects implies a common physical origin. The lines are predictions of the simplified model for spins of $a_* = 0.2$ (dot-dashed), 0.5 (dashed) and 0.998 (solid) with r_o ranging from r_i to 100 and $r_i = r_{bw}$. For the blue lines, we assume the viscous frequency to be proportional to the Keplerian frequency. For the green lines, we assume $f_{visc} = Br^{-m}f_k$ where $B = 0.03$ and $m = 0.5$ and find good agreement with the trend in the data.

$$f_{LT} = f_k \left[1 - \sqrt{1 - \frac{4a_*}{r^{3/2}} + \frac{3a_*}{r^2}} \right] \quad (2)$$

is the point particle Lense-Thirring precession frequency for a dimensionless spin parameter a_* (Merloni et al 1999). Here, r is dimensionless, expressed in units of $R_g = GM/c^2$. Solving this assuming a power law form for surface density in the hot flow $\Sigma \propto r^{-\zeta}$ between an inner and outer radius for the hot flow r_i and r_o (Fragile et al 2007, IDF09) gives

$$f_{QPO} = \frac{(5 - 2\zeta)}{\pi(1 + 2\zeta)} \frac{a_*[1 - (r_i/r_o)^{1/2+\zeta}]}{r_o^{5/2-\zeta} r_i^{1/2+\zeta} [1 - (r_i/r_o)^{5/2-\zeta}]} \frac{c}{R_g}. \quad (3)$$

Hence this model predicts the relation between f_{QPO} and f_b which can be compared to the multiple observations of these frequencies in both black holes and neutron stars (e.g. Wijnands & van der Klis 1999; Klein-Wolt & van der Klis 2008). The observed relation is continuous, implying that these frequencies show the same behavior in both sources, i.e. that neither can depend strongly on any property of the neutron star surface but are instead set by the accretion flow itself. We re-plot this data in Figure 1, normalizing the frequencies by mass for a fiducial mass of 1.4 and $10M_\odot$ for neutron stars (red triangles) and black holes (black circles), respectively. This shows even more clearly that the two different types of object show the same observed relation between these frequencies as they now occupy the same range.

The blue lines show the prediction of the toy model, where the hot flow has constant $\alpha = 0.2$ and $h/r = 0.2$, surface density constant with radius (i.e. $\zeta = 0$: Fragile et al 2007) between r_o and r_i , where r_i is given by the bending wave radius. Warps in a large scale height flow are communicated via bending waves which have wavelength $\lambda \propto r^{9/4}$ and so are smooth at large r and oscillatory at small r . The bending wave radius ($r_i = 3.0(h/r)^{-4/5}a_*^{2/5}$; Fragile et al 2007; 2009; Fragile 2009; IDF09) marks the transition between the two regimes. We show $a_* = 0.2$ (dot-dashed), $a_* = 0.5$ (dashed) and $a_* = 0.998$ (solid). While this very simple model

predicts frequencies which are fairly close to the observations, it is clear that the gradient of this model in log space is different from that observed.

Plainly the assumptions above are very simplistic. Global analytic models of the hot flow with a standard α viscosity do not have $f_{visc} \propto f_K$ as they depart from the self-similar solutions at $r < 100$ due to the requirement that the flow becomes supersonic (Narayan, Kato & Honma 1997; Gammie & Popham 1998). Full numerical simulations also show that α is not constant (e.g. Fragile et al 2007; 2009). Ingram & Done (2010) also suggest that ζ can change in neutron stars as the material piles up onto a boundary layer. However, the similarity between the mass scaled frequencies seen in neutron stars and black holes shown in Fig. 1 make this now seem unlikely to be an important effect as it would not affect the black holes.

Here then we simply assume that $\alpha(h/r)^2$ is a power law function of radius, so that $f_{visc} = Br^{-m}f_K$. We choose values for B and m which allow us to match the data in Figure 1. We see good agreement with the observations for $B = 0.03$ and $m = 0.5$ (green lines), again for $a_* = 0.2$ (dot-dashed), $a_* = 0.5$ (dashed) and $a_* = 0.998$ (solid). We use this specific prescription for the viscous frequency in the following section.

3 THE FULL MODEL

We consider a model where local fluctuations in the mass accretion rate of the flow propagate down towards the central object (e.g. L97; K01). Our method mainly follows that of AU06, with a few small differences.

We split the flow into annuli, characterized by a radius r_n and width dr_n , with logarithmic spacing so dr_n/r_n is a constant for all annuli from r_o to r_i . As $f_{visc} \propto r^{-(m+3/2)}$ in our prescription, constant dr_n/r_n also implies constant df/f which AU06 show is the feature required to produce a linear sigma-flux relation.

MRI fluctuations throughout the flow generate variability in all quantities. Fluctuations in mass accretion rate will most likely be damped by the response of the flow on timescales shorter than the local viscous timescale. We therefore assume that the generated power spectrum of mass accretion rate fluctuations at radius r_n is given by a zero centred Lorentzian cutting off at the viscous frequency

$$|\tilde{m}(r_n, f)|^2 \propto \frac{1}{1 + (f/f_{visc}(r_n))^2} \quad (4)$$

where $f_{visc} = -\frac{1}{R_g}v_r/r = Br^{-m}f_K$ as discussed at the end of section 2 and a tilde denotes a Fourier transform.

We start at the outermost annulus, so $r_1 = r_o$, and generate the time dependent fluctuations in mass accretion rate, $\dot{m}(r_1, t)$, from equation 4 using the method of Timmer & Koenig (1995). We normalize each $\dot{m}(r_n, t)$ to have a mean of unity and fractional variability $\sigma/I = F_{var}\sqrt{N_{dec}}$ where F_{var} is the fractional variability per decade in radial extent and N_{dec} is the number of annuli per decade in radial extent. Thus the mass accretion rate across the first annulus is $\dot{M}(r_1, t) = \dot{M}_0\dot{m}(r_1, t)$ where \dot{M}_0 is the mean mass accretion rate. This then propagates inward to the second annulus, travelling a distance dr_1 , which takes a time $t_{lag} = R_g dr_1/v_r(r_1)$. When it arrives at r_2 , it has been filtered by the response of the flow which we take from Psaltis & Norman (2000) to get

$$\tilde{\dot{M}}_f(r_n, f) \propto \frac{\tilde{M}(r_n, f)}{\sqrt{1 + [(dr_n/r_n)(f/f_{visc}(r_n))]^2}}. \quad (5)$$

The mass accretion rate at the n^{th} annulus is then given by

$$\dot{M}(r_n, t) = \dot{M}_f(r_{n-1}, t - t_{lag})\dot{m}(r_n, t) \quad (6)$$

where $t_{lag} = R_g dr_n/v_r(r_n)$. However, equation 5 only filters out fluctuations on much shorter timescales (by a factor dr/r) than the typical timescales generated in the annulus (equation 4) and so we can say $\tilde{\dot{M}}_f(r_n, f) \approx \tilde{M}(r_n, f)$ to a very good approximation. The mass accretion rate at the n^{th} annulus is therefore given by

$$\dot{M}(r_n, t) = \dot{M}(r_{n-1}, t - t_{lag})\dot{m}(r_n, t), \quad (7)$$

until the N^{th} annulus which is r_i .

To transform this into a light curve requires an emissivity, $\epsilon(r)$ such that the luminosity from each annulus is given by $dL(r, t) = 1/2 \dot{M}(r_n, t)\epsilon(r)r_n dr_n c^2$ where we assume the emissivity $\epsilon(r) \propto r^{-\gamma}b(r)$ where $b(r)$ is a boundary condition. For a Newtonian thin disc, $\gamma = 3$ and we have the stress free inner boundary $b(r) = 3(1 - \sqrt{r_n/r_i})$ but we note that the large scale magnetic fields present in the large scale height flow can give a stressed inner boundary condition $b(r) = 1$ (Agol & Krolik 2000; Beckwith Hawley & Krolik 2008). We also allow γ to be a free parameter as the emission need not exactly follow the radial dependence of gravitational energy release as long as the *total* energy release is gravitational. A different emissivity for different energy bands gives a way for the model to predict frequency dependent time lags between hard and soft X-ray bands (K01; AU06). This will be the subject of a subsequent paper.

4 THE FIDUCIAL MODEL

Figure 2a shows 20 s of the resulting light curve for a fiducial set of input parameters for a black hole mass of $M = 10M_\odot$ and a spin of $a_* = 0.5$. We assume $r_i = 2.5$, $r_o = 20$, $F_{var} = 0.4$, $B = 0.03$, $m = 0.5$, $\gamma = 4.5$ with a stressed inner boundary condition (see Section 2). We calculate the light curve with 2^{22} time points, corresponding to ~ 4096 s (a typical length for an RXTE observation) of data on a time binning of 0.00097 s, and 30 radial bins.

Figure 2b (red) shows the PSD of this light curve, while the black and green points show the effect of changing the number of radial bins to 10 and 100, respectively. Clearly, the high frequency power is not well resolved with only 10 radial bins, while the difference between 30 and 100 is very small. Hence in all that follows, we use 30 radial bins for each simulation.

The PSD shows the same characteristic broadband noise features as are seen in the power spectra of black hole binaries, namely band limited noise, with low and high frequency breaks, peaking between 0.1-10 Hz. Figure 2c shows the rms-flux relation for the fiducial light curve, derived from splitting this into 4s segments. As with the data (Uttley & McHardy 2001), we see a large scatter before binning (gray points) but, after binning (red crosses), we retrieve a linear flux-rms relation (AU06).

5 THE TRUNCATED DISC/HOT INNER FLOW MODEL

The major prediction of the truncated disc/hot inner flow model is that the spectral softening as the source brightens from a low/hard through to intermediate states is caused by the truncation radius

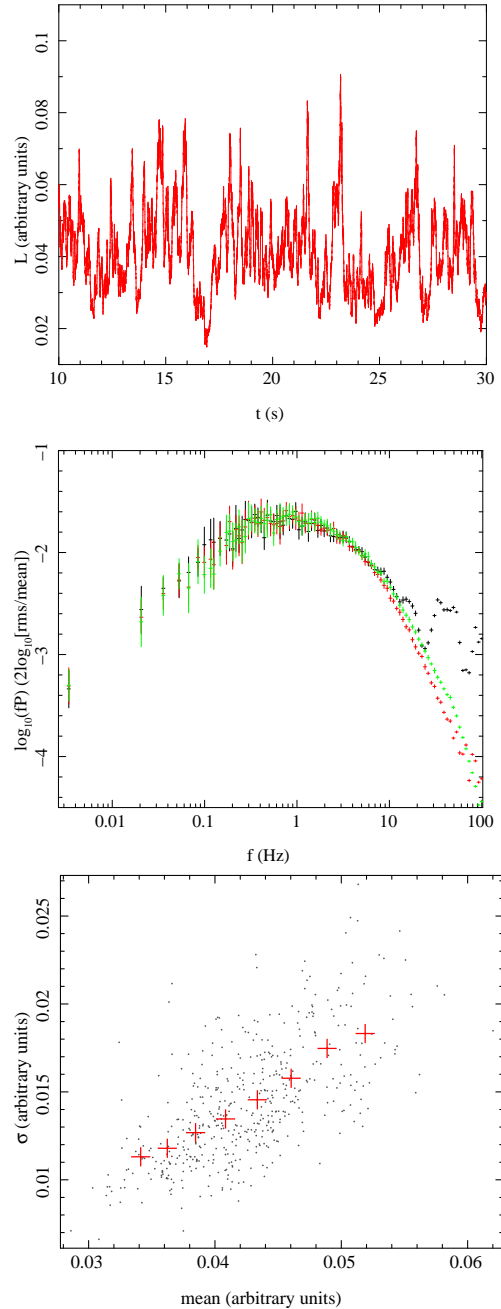


Figure 2. *Top (a):* A 20 second section of the simulated light curve. *Middle (b):* The simulated power spectral density calculated using 10 (black), 30 (red) and 100 (green) radial bins. We see that, 10 bins is not enough to resolve the high frequency power but 30 bins is a good approximation. *Bottom (c):* The rms-flux relation for the light curve shown. We see that this is linear as observed.

of the thin disc moving inwards (e.g. DGK07; Gierlinski, Done & Page 2008). This radius also sets the outer edge of the hot flow, so this predicts that r_o decreases also.

Figure 3 shows the predicted PSD for $r_o = 50, 20$ and 10 , as required to match the energy spectral evolution (and low frequency QPO: IDF09), with all other parameters held constant at the fiducial model values described above. The model *predicts* that decreasing the outer radius of the hot flow leads to less low frequency power, while the high frequency power remains constant. This is precisely

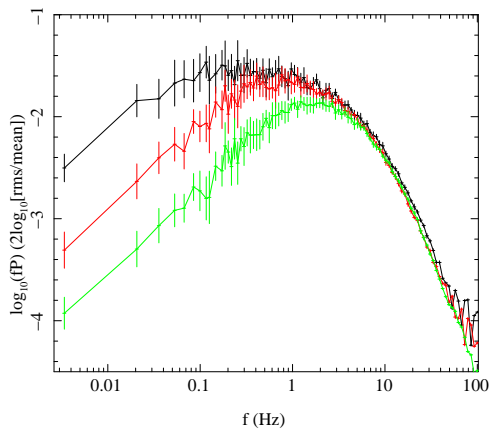


Figure 3. PSD calculated using the fiducial parameters with $r_o = 50$ (black), 20 (red) and 10 (green) with total fractional variability generated per decade in radius, F_{var} , held constant. This has the same characteristics as the observed PSD of the data as the source softens from a low/hard to intermediate state, namely that the low frequency power drops while the high frequency power remains constant.

what is seen in the PSD of the data (DGK07; Gierlinski, Nikolajuk & Czerny 2008).

This is the first physical model of the power spectral behavior which naturally reproduces the observations. The low frequency break is close to the frequency of the viscous timescale at r_o , as proposed by e.g. by Churazov et al (2001); Gilfanov & Areief (2005); DGK07; Ingram & Done (2010). However, the high frequency break is *not* at the viscous frequency at r_i . We explore the origin of the high frequency break below.

5.1 Effect of propagation on the PSD shape

Figure 4a shows a model where the variability at each radius is a Lorentzian at the local viscous frequency (see equation 4), but with no propagation so there is no causal connection between annuli. We show the PSD of the resulting $\dot{m}(r_n, t)$ functions from 5 of the 30 individual radial annuli, from r_o to r_i as the gray lines on Figure 4a. These peak, as expected, at $f_{visc}(r_o)$ and $f_{visc}(r_i)$. The total variability (red) is an emissivity weighted sum of these fluctuations, but since they are uncorrelated, the effect of this is to strongly dilute the total variability seen. This total PSD does have $f_h \approx f_{visc}(r_i) \sim 12\text{Hz}$ as our emissivity weighting strongly favors the smallest radii, but $f_b > f_{visc}(r_o)$ ($\sim 10\text{Hz}$ and $\sim 0.3\text{Hz}$ respectively). In fact, to achieve $fP_f \propto f^0$ as observed, we would have to assume a completely flat emissivity profile, which seems very unlikely. More fundamentally, such uncorrelated fluctuations *cannot* reproduce a linear rms-flux relation.

This is in sharp contrast to a model where fluctuations propagate down in radius. The resulting PSD from the same set of radii are shown in Figure 4b, where the power in each annulus increases strongly with radius as the MRI power generated in each annulus is modulated by the propagating fluctuations from all radii prior to it. The red line shows the resulting emissivity weighted power spectrum from the total flow assuming that time lags between radii are negligible. This preserves the maximum correlation between variability at different annuli i.e. gives the least dilution between fluctuations in different annuli. This is very different to that in Figure 4a, both in normalization and shape. The normalization is dramatically enhanced because the long timescale fluctuations are correlated to-

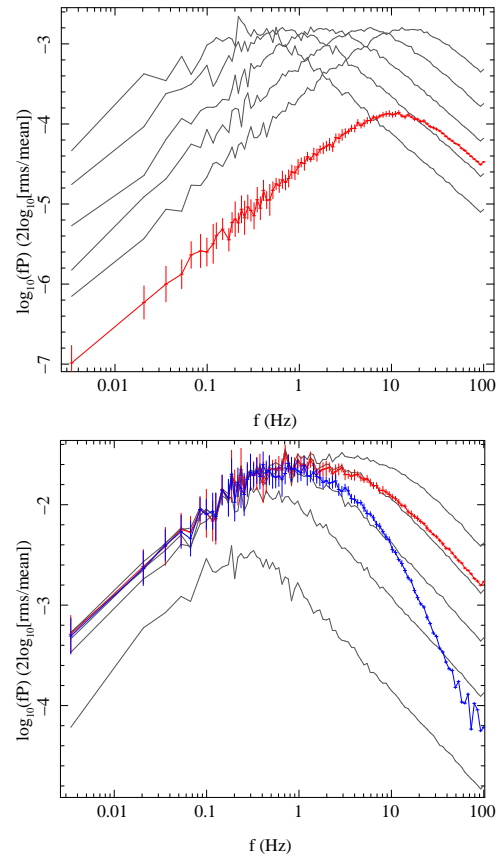


Figure 4. *Top (a):* The gray lines are the power spectra of 5 simulated $\dot{m}(r_n, t)$ functions. We simulate 30 of these functions but, for clarity, only plot 5 without showing the errors. The red line is the PSD of the light curve created by assuming there to be no propagation (i.e. $\dot{M}(r_n, t) = \dot{m}(r_n, t)$) and an emissivity index of 4.5. Because the functions we sum over are uncorrelated, the PSD of the light curve looks like the (weighted) sum of the 100 PSDs with the only difference being the normalization. *Bottom (b):* The gray lines are now the power spectra of $\dot{M}(r_n, t)$ functions, i.e. we now allow propagation. These are correlated at low frequencies but not at high frequencies allowing the model to reproduce the observed linear sigma-flux relation. The red line is the PSD of the light curve if we do not consider the propagation time between annuli (i.e. $t_{lag} = 0$) and the blue line results if we do consider the propagation time. We see that the red line differs from the top plot in 2 ways: the normalization is much higher and high frequency noise is lost. However, much more high frequency noise is lost for the blue line indicating that considering lags reduces high frequency noise. These plots illustrate that the prediction from shot noise models such as the top plot that the observed high frequency break is the viscous frequency at the inner radius breaks down once we consider a more advanced model capable of reproducing other observational properties.

gether, so at low frequencies the power from different radii add together as they are in phase. This gives $f_b \approx f_{visc}(r_o) \sim 0.3\text{Hz}$ as the correlated variability weighting to larger radii is stronger than the emissivity weighting to smaller radii. However, at the fastest timescales, the power is mainly generated at the smallest radii, so it does not correlate with any other fluctuations generated at larger radii, so is not enhanced in the same way.

The blue line shows how time delays dramatically change the high frequency break as the propagation time prevents the mass accretion rate from two consecutive annuli from being correlated on time scales shorter than t_{lag} . This reduces the correlation between the fastest timescale variability, strongly suppressing high

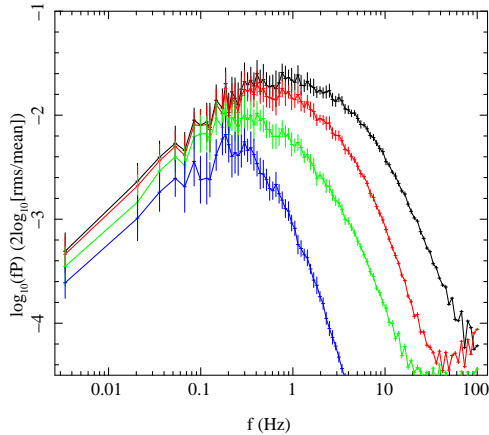


Figure 5. The PSD calculated assuming $b(r) = 1$ and $\gamma = 4.5$ (black), $b(r) = \text{stress free}$ and $\gamma = 4.5$ (red), $b(r) = \text{stress free}$ and $\gamma = 3$ (green), all with $r_i = 2.5$. The blue points are for $b(r) = \text{stress free}$, $\gamma = 3$ and $r_i = 6$. This illustrates that we can reduce the predicted high frequency noise by changing boundary condition, emissivity index or inner radius.

frequency power. Thus in the propagating fluctuation model, the low frequency break is $f_b \approx f_{visc}(r_o)$ but $f_h \ll f_{visc}(r_i)$.

5.2 Emissivity and boundary condition

We use an emissivity to translate the fluctuations in mass accretion rate to a luminosity. This emissivity is in two parts, firstly a power law dependence in radius, and secondly a boundary condition. Our fiducial model parameters have $\gamma = 4.5$ and a stressed boundary condition, $b(r) = 1$. This emissivity peaks at r_i , so fluctuations from the very smallest radii are given most weight.

Figure 5 compares this (black line) with results using the same power law radial dependence, but with a stress-free inner boundary condition (red line), $b(r) = 3(1 - \sqrt{r/r_i})$. This emissivity goes to zero at the innermost radius, so the highest frequency fluctuations are strongly suppressed. However, this also has a more subtle effect on the region between the two breaks, as there is a gradual decrease in weighting of fluctuations below $r = 2r_i$, and a stronger weighting to the fluctuations at larger radii, giving the tilt between f_b and f_h .

This effect is similar to that of changing the radial dependence of the emissivity. The green line shows $\gamma = 3$ with a stress-free boundary condition, showing an even stronger tilt to the PSD between f_b and f_h (green). However, it is also similar to changing the inner radius of the flow. The blue line in Figure 5 shows the resulting PSD from $\gamma = 3$ and a stress-free inner boundary condition with $r_i = 6$. Thus there are degeneracies between the two parts to the emissivity and the inner radius, making it unlikely that they can all be uniquely constrained by the observed PSD.

It is clear from this analysis that while the low frequency break is fairly strongly linked to the viscous timescale of the outer radius of the hot flow (as assumed in section 2), the high frequency break is rather more complex, depending on propagation correlations, emissivity, boundary condition and inner radius in addition to the viscous timescale. This makes it difficult to directly associate the high frequency break with any physical parameter of the models. Instead, we now use the additional information from the QPO to remove some of the degeneracies inherent in this model for the broadband noise.

6 THE QPO: PRECESSION AND SURFACE DENSITY

For our fiducial model, we used the observed relation between the low frequency break and LF QPO to set the radial dependence of the viscous timescale, assuming that the low frequency break was set by the viscous timescale at r_o and that the QPO was Lense-Thirring precession of the entire hot flow from r_o to r_i (Section 2). This assumed that the surface density of the hot flow, $\Sigma = \Sigma_0 r^{-\zeta}$ between r_o and r_i , with $\zeta = 0$. However, the broadband noise model described above calculates a self-consistent surface density as mass conservation implies

$$\dot{M}(r_n, t) = -2\pi r_n v_r(r_n) \Sigma(r_n, t), \quad (8)$$

(Frank, King & Raine 1992) where v_r is now expressed in units of c , \dot{M} in units of \dot{M}_0 , Σ in units of $\dot{M}_0/(cR_g)$ and r in units of R_g . Using our velocity prescription, we can then easily show

$$\Sigma(r_n, t) = \frac{\dot{M}(r_n, t) r^{m-1/2}}{B}. \quad (9)$$

This means that, for the time averaged surface density, $\zeta = m - 1/2$ giving extra physical motivation for the parameters used in section 2 ($\zeta = 0$ and $m = 1/2$).

Figure 6 shows $\Sigma(r_n)$ plotted at a number of different times (0, 256, 512, ..., 1792 s) along with the corresponding $\dot{M}(r, t)$ function. $\dot{M}(r, t)$ is quite clearly more variable at small r . This is because we have assumed the variability *generated* in each logarithmic annulus to be the same but annuli at smaller radii include also the fluctuations that have propagated down from large r and so the *emitted* variability is greater (see Figure 4b). We do not see a drop off in surface density at the bending wave radius like that seen in simulations (e.g. Fragile 2009) because we assume that the infall velocity can be given by a power law. It is clear that, for the surface density drop off at a given point, the infall velocity must accelerate at that point. In a future paper, we will investigate this model with a more advanced velocity prescription.

Therefore the broadband noise model above, set by r_i , r_o and F_{var} *predicts* the QPO frequency at any point in time. The fluctuations in surface density with time *predict* that the QPO frequency changes, i.e. it is quasi-periodic rather than truly periodic. However, the precession frequency will not respond instantaneously to these changes, as their effect is only communicated across the entire hot flow by bending waves. These travel at the sound speed, faster by a factor $\sim \alpha$ than the viscous timescale across the region, so we calculate the QPO frequency every ~ 4 s rather than at every point. We then average these values to get the predicted QPO frequency, f_{QPO} , and use the dispersion around this to set the *r.m.s.* variance of these QPO frequencies, σ_{QPO} .

Fig. 7 shows σ_{QPO}/f_{QPO} as a function of f_{QPO} as r_o varies from 300–10 in the fiducial model. This decrease in r_o not only leads to an increase in QPO frequency, but also to a decrease in the QPO width, or equivalently, an increase in its coherence/quality factor $Q = f_{QPO}/\sigma_{QPO}$. This correlation is well known in QPO data from BHB (e.g. Belloni, Psaltis & van der Klis 2002; Rao et al 2010). Our model provides the first physical explanation for this effect as the smaller the radial extent, the higher the QPO frequency, but also the smaller the fluctuation power, giving smaller jitter in frequency. The red squares in Fig 7 show the *observed* frequency and width of the QPO from data from the 1998 rise to outburst of the BHB XTE J1550-564 (see section 7). The model matches the trend in the data fairly well, and forms a lower limit to the width of the QPO. However, other effects such as the on-time of the QPO (see Lachowicz & Done 2010) can decrease the coherence of the signal, so here we simply use the data to determine the

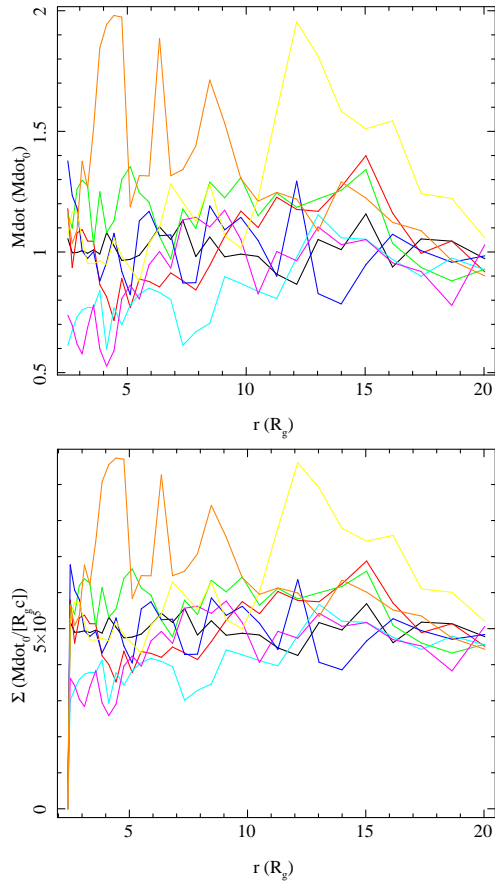


Figure 6. *Top:* Mass accretion rate as a function of radius shown here at a number of different times. *Bottom:* Surface density as a function of radius shown at the same times as the lines of corresponding colour in the top plot. This is calculated by applying mass conservation in the flow. The dotted line in the bottom plot represents the bending wave radius for $a_* = 0.5$ and $h/r = 0.2$ which seems to trace the point where the surface density begins to drop off.

QPO width (parametrized as a quality factor $Q = f_{QPO}/\sigma_{QPO}$) after using the broadband noise surface density to determine the QPO frequency, f_{QPO} .

The model also predicts another correlation, one between the QPO frequency and flux on short timescales. The top plot of Figure 8 shows this for the fiducial model (i.e. $r_o = 20$), with precession frequency calculated every 4s together with the instantaneous luminosity at that time. After binning (red crosses), there is a clear linear relation between the two. This happens because both the QPO frequency and the luminosity depend on the mass accretion rate fluctuations. A perturbation in mass accretion rate at large r will lead to a perturbation in the surface density. This will reduce the precession frequency but will have little effect on the luminosity because the emissivity is quite steeply weighted towards small r . Later on, this perturbation will have propagated inwards to small r where it has the effect of increasing the precession frequency, but now also has much more of an effect on the luminosity. Heil et al (2011) have recently discovered this correlation in data from the 1998 rise to outburst of XTE J1550-564 (the same data as we will be considering in section 7). They also find that the gradient of this relation is steeper for observations with a higher QPO frequency. This is also predicted by the model as illustrated in the bottom plot of Figure 8 where we have measured the gradient of the

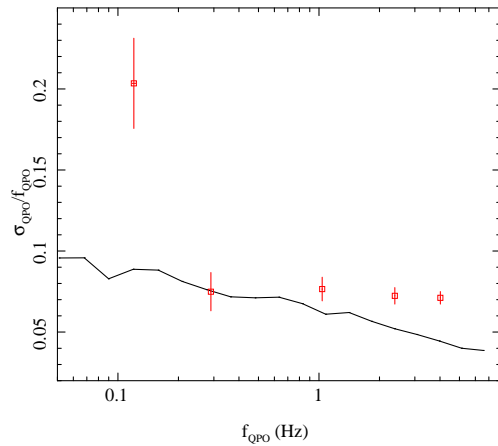


Figure 7. Fractional variability of the precession frequency plotted against the average precession frequency (black line). These are calculated by measuring the precession frequency every 4s for a number of different truncation radii, ranging from 300 – 10, and taking the average and standard deviation over a 2048s duration. The red squares show the observed QPO width and frequency in data from the 1998 rise to outburst of XTE 1550-564. We see broad agreement with the data, however, other effects such as on-time of the QPO can decrease the coherence of the signal so we note that we are only able to predict a lower limit for the width of the QPO

f_{QPO} - L relation and the average QPO frequency for 11 different r_o values. There is clearly a very strong correlation as is seen in the data. This is because an *absolute* change in precession frequency depends on a *fractional* change in mass accretion rate whereas an *absolute* change in luminosity depends on an *absolute* change in mass accretion rate. The same absolute change in mass accretion rate at a given radius and time constitutes a larger *fractional* change for small r_o than for high r_o . Therefore the luminosity will experience exactly the same change in both instances but the precession frequency will undergo a larger change when r_o is smaller. The fact that these are *predicted* properties of the model constitutes strong support for its validity.

In the following section, we will fit the PSD from our model to data. For this, we will need to predict a *shape* for the QPO light curve as well as a frequency. The data show that the QPO has a power spectrum which can be represented by a Lorentzian at the fundamental frequency, f_{QPO} , together with its second and third harmonic and sub-harmonic i.e. at $2f_{QPO}$, $3f_{QPO}$ and $1/2f_{QPO}$ (e.g. Belloni, Psaltis & van der Klis 2002). Our model for the QPO in terms of Lense-Thirring precession *predicts* the shape of the modulation of the emission from the hot flow via variation of projected area, self-occultation and seed photons (IDF09). We will explore this further in a later paper (Ingram, Done & Źycki in prep), but here we simply assume that all the harmonics have the same quality factor, Q , and allow the power in each harmonic to be a free parameter. We then generate a QPO light curve, L_{QPO} , using these narrow Lorenzians as input to the Timmer & Koenig (1995) algorithm, and add this to the light curve already created for the broadband noise.

We show an example of the final predicted PSD in Figure 9, using the fiducial model parameters with $r_o = 50$ (black), 20 (red) and 10 (green). For clarity, we have set the normalization of all the harmonics other than the fundamental to 0, set the width of the QPO using the model prediction of σ_{QPO}/f_{QPO} , and set its rms power $\propto 1/r_o$. These PSD show all the main features seen in the

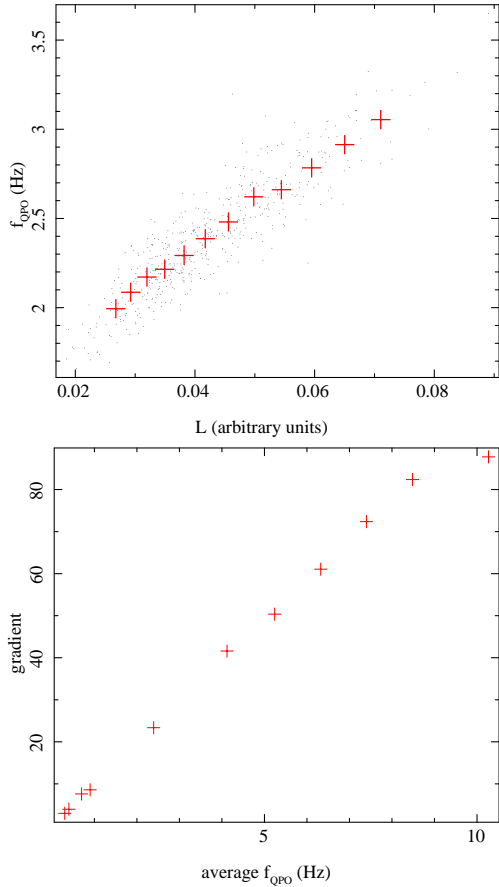


Figure 8. Precession frequency plotted against luminosity, where both are calculated at 4s intervals using the fiducial model parameters (gray points). After binning (red crosses), we clearly see a linear relationship between the two quantities. This relationship has recently been discovered in data from the 1998 rise to outburst of XTE J1550-564 (Heil et al in print), demonstrating the substantial predictive power of this model.

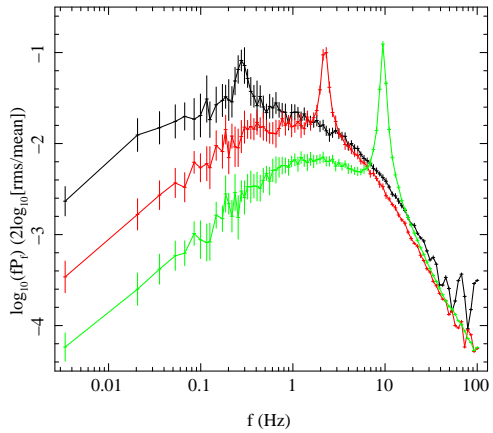


Figure 9. The full PSD calculated using the fiducial model parameters with $r_o = 50$ (black), 20 (red) and 10 (green). Here, the QPO is represented by a Lorentzian centred at the precession frequency with the width set by the r.m.s variance in precession frequency (see text).

data during spectral transitions of BHB (Gierlinski, Nikolajuk & Czerny 2008).

7 FITTING TO XTE J1550-564

We now have a model which can produce both the broad band noise and QPO self consistently from the same changing geometry as required by the corresponding evolution of the energy spectra, namely a changing outer radius of the hot flow (set by the changing inner radius of the thin disc). This model gives the major correlation between the low frequency break and low frequency QPO. The propagating fluctuations naturally give the rms-flux relation, while the QPO model also gives a framework in which to understand the increase in coherence of the QPO with frequency, and even the short timescale correlation of the QPO frequency with flux. Plainly, the next step is to use this model to fit real data.

We use RXTE data from the 1998 outburst of XTE J1550-564 (Remillard et al 2002; Sobczak et al 2000; Rao et al 2010; Wilson & Done 2001). We look at 5 specific observations with observational IDs: 30188-06-03-00, 30188-06-01-00, 30188-06-01-03, 30188-06-05-00 and 30188-06-11-00; hereafter observations 1-5 respectively. We only consider energy channels 36-71 (corresponding to 10-20 keV) in order to avoid disc contamination.

In all our results so far we have shown power spectra produced by averaging the logarithm of the periodogram as Papadakis & Lawrence (1993) show that, for a red noise variability process, the error estimate converges to Gaussian with only ~ 20 samples, rather than the ~ 50 required for averaging the linear power estimates. Our simulations average over $M = 32$ samples of the PSD but the number of segments from the real data cannot be chosen as they are simply set by the length of the available data. These give $M = 41, 26, 13, 14$ and 14 respectively, implying that the errors on the PSD from the data are only approximately Gaussian. A further complication is that the error distribution of the periodogram is dependent on the shape of the underlying power spectrum (e.g. Mueller, Madejski & Done 2004; Mueller & Madejski 2009) meaning that even $M = 20$ may not be enough to give Gaussian errors in this particular case. Nonetheless, we choose to use χ^2 minimization for simplicity, but we then do *a posteriori* checks on the goodness of fit using the rejection probability method of Uttley et al (2002) and Markewicz et al (2003). This entails first calculating

$$\chi_{dis}^2 = \frac{1}{M} \sum_{k=1}^M \sum_f \frac{(\overline{P}_{sim}(f) - \log_{10}[P_{obs,k}(f)])^2}{(\Delta \overline{P}_{sim}(f))^2} \quad (10)$$

where $\overline{P}_{sim}(f)$ is the logarithmically smoothed simulated periodogram, with error $\Delta \overline{P}_{sim}(f)$, to be compared to M raw observed periodograms, $P_{obs,k}(f)$. We then re-simulate many (512) light curves and calculate many different values of

$$\chi_{dis}^2(sim) = \frac{1}{M} \sum_{k=1}^M \sum_f \frac{(\overline{P}_{sim}(f) - \log_{10}[P_{sim,k}(f)])^2}{(\Delta \overline{P}_{sim}(f))^2}. \quad (11)$$

The rejection probability, P_{rej} , is given by the percentile of $\chi_{dis}^2(sim)$ values which are lower than the one χ_{dis}^2 value. For example, if 128 of the $\chi_{dis}^2(sim)$ values were smaller than the one χ_{dis}^2 value, the rejection probability is 25%. This means there is a 25% chance that the observed light curve was generated by a different underlying variability process than the model.

One aspect of using real data is that there are uncertainties associated with each point on the light curve. Since we use the logarithmically averaged PSD we need the power to be positive definite

so we cannot do white noise subtraction of the data PSD. Instead we add white noise to the simulation, and compare this with the total (including noise) power spectrum of the real data (see also Uttley et al 2002).

We incorporate our model for the power spectrum into XSPEC, using the local model functionality. Our model outputs the logarithmically averaged total (white noise included) periodogram as a function of Fourier frequency rather than the more familiar flux as a function of energy. We then fit this to the similarly logarithmically averaged total power spectra from the real data. The model parameters are the physical parameters governing the behavior of the flow. The most fundamental of these is the relation governing the viscous frequency at any radius. We have parametrized this as a power law function of the Keplerian frequency at each radius, $f_{visc} = Br^{-m}f_{kep}(r)$, but the parameters B and m are unknown, so are free in the fits, as is F_{var} , the intrinsic level of the MRI fluctuations in mass accretion rate. Then there are the geometric parameters r_o and r_i , where r_i also couples to the emissivity, both in terms of the index γ and the boundary condition (either stressed or stress free). The combination of r_o , r_i and the surface density profile fixes the QPO frequency, but we leave its width (parametrized as a quality factor, Q) and normalization as free parameters. We also allow the normalization of the second, third and subharmonic to be free parameters, but fix these to have the same Q as that of the fundamental. The final free parameter is the normalization of the simulated white noise level, σ_{lc} , which we then subtract from both data and model in order to plot results.

The truncated disc model predicts that r_o is the major parameter which changes across this transition, where r_i remains fixed. Hence we fit all 5 power spectra simultaneously in XSPEC, with r_i tied across all 5 datasets. Because of the correlation between r_i and both parts of the emissivity (see section 5.2), we choose to compare results with some of these parameters fixed at different values.

7.1 Fit results

7.1.1 Stressed inner boundary

In this section we fit our model to the 5 observations considered assuming a stressed inner boundary condition. Figure 10 displays the best fit models and data with the inner radius and emissivity index required to be constant across the 5 observations. These appear by eye to be good fits, and this is confirmed by their rejection probabilities of 51%, 30%, 26%, 12% and 16% for observations 1–5, respectively. We find the inner radius to be $r_i = 2.45$ which, although low, is greater than the horizon of the black hole ($r_H \approx 1.87$ for our chosen $a_* = 0.5$). The truncation radius moves from $r_o = 75.7 - 13.6$. However, the fit requires that the power law index governing the viscous frequency, m , increases across the observations, from $m = 0.46 - 1.016$. We will discuss the significance of this in section 8.

7.1.2 Stress free inner boundary

In the previous section, we recovered an inner radius fairly close to the horizon ($r_i = 2.45$) for fits with a stressed boundary condition. This assumption implies a causal connection to material closer in which, given the proximity of the emission to the horizon, may not be physical. Hence the stress free inner boundary condition may be more physically appropriate. We repeat the fits assuming this, with results shown in Figure 11. We recover an even lower inner radius ($r_i = 2.0$), and similar values for the truncation radius

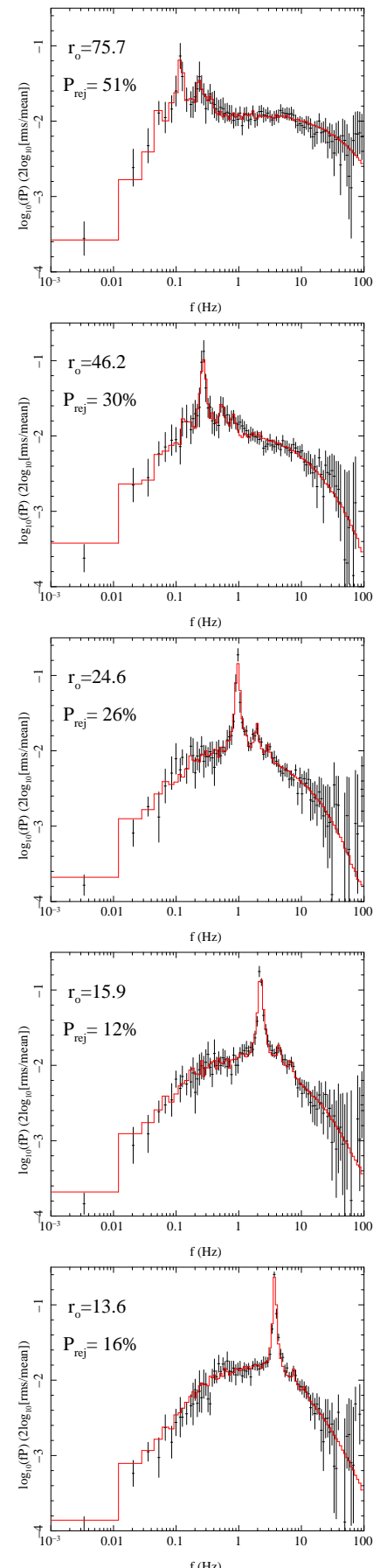


Figure 10. Results of fits for $\gamma = 4.15$ and $b(r) = 1$ plotted with the white noise subtracted. The truncation radius, r_o , and rejection probability, P_{rej} , are included in the plots. Here $r_i = 2.45$ and $m = 0.46 - 1.016$.

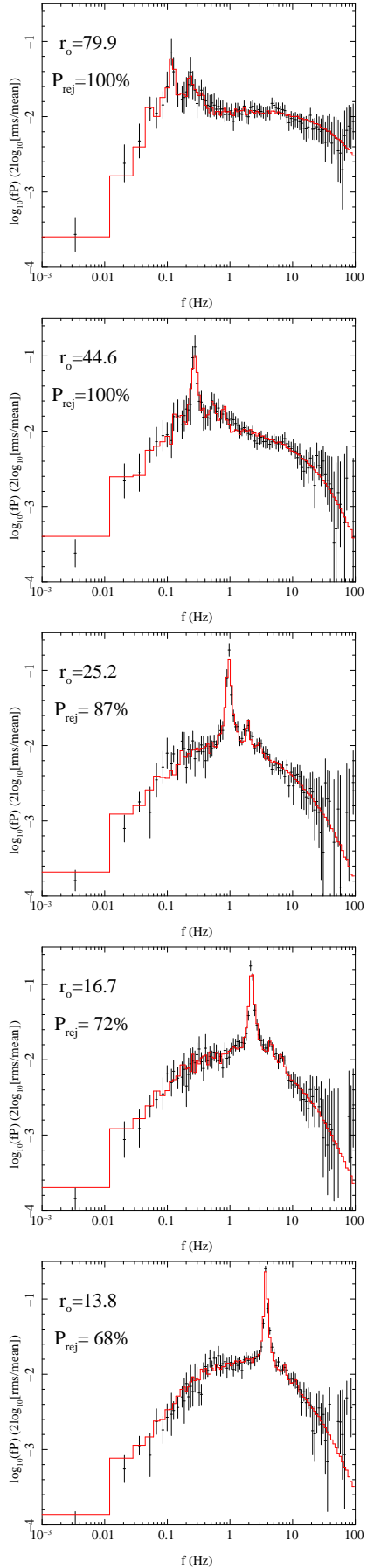


Figure 11. Results of fits for $\gamma = 5.06$ and stress free inner boundary plotted with the white noise subtracted. The truncation radius, r_o , and rejection probability, P_{rej} , are included in the plots. Here $r_o = 2.00$ and

($r_o = 79.9 - 13.8$) and power law index governing the viscous frequency ($m = 0.44 - 1.30$). By eye, these again appear to be excellent fits; in fact they look nearly identical to Figure 10 and have only a marginally higher χ^2 value. However, these have rejection probabilities of 100%, 100%, 87%, 72% and 68% for observations 1 – 5 respectively, so they are all statistically unacceptable. A rejection probability of 100% means that all of the 512 simulated PSDs had $\chi^2_{\text{dis}}(\text{sim})$ smaller than the one ‘observed’ χ^2_{dis} , making it extremely unlikely that the observed data is part of the simulated distribution.

This discrepancy between χ^2 and rejection probability points to the complex nature of the statistics of the periodogram. We discuss this in more detail in the Appendix, but here we simply note that these results do *not necessarily* mean that there is no good fit for the stress free version of the model: they just mean that the real best fit parameters do not give the lowest χ^2 . The previous fits with a stressed boundary condition also may not be the best fit in terms of rejection probability, the difference is that with the stressed boundary condition the minimum χ^2 solution was also a statistically acceptable fit on rejection probability. We will explore this in more detail in a future paper (Ingram & Done, in preparation)

However, as the fits appear to be good by eye, it seems very likely that there should be a set of parameters very close to the ones that minimize χ^2 that give much lower rejection probabilities.

8 DISCUSSION

Although the statistical complexities of the periodogram currently limit the model fitting to data, the parameters we derive are still most likely very close to the actual best fit parameters, and all four fits in the previous section came out with similar results for r_o and the viscous frequency radial dependence. While the change in r_o is predicted from the truncated disc/hot inner flow geometry proposed to model the correlated spectral changes, the change in viscous frequency radial dependence is not.

There are two (at least) scenarios in which this could occur. Firstly, this could indicate that the viscous frequency is well approximated by a power law but that the form of this changes as the truncation radius moves inwards (as assumed in Ingram & Done 2010 for the neutron star power spectra). There is currently no theoretical model in which this occurs. A more attractive (to us) possibility is that a power law is a poor approximation for the viscous frequency and, as the truncation radius moves, the power law that best approximates the true shape of the viscous frequency with radius changes. This would imply that there is a stationary function $f_{\text{visc}}(r)$ (and by extension $v_r(r)$) which would allow this model to fit all 5 observations with only a change in r_o . We note that exactly this behavior is predicted in global simulations of an ADAF as the flow has to accelerate strongly to pass through a sonic point (e.g. Narayan, Kato & Honma 1997; Gammie & Popham 1998). These models give an in-fall velocity $v_r(r)$ which is well approximated by a quadratic in log space (see Fig 1 in Gammie & Popham 1998). This will also allow the model to display a drop off in surface density in agreement with simulations as discussed in section 6. Approximating such a velocity law by a power law of index m will result in m increasing as the radial extent of the flow decreases, similar to the observed trend. We will explicitly fit such models in a later paper (Ingram & Done in preparation).

9 CONCLUSIONS

The truncated disc/hot inner flow model designed to describe the spectral evolution of BHB can also give a self consistent geometry in which to model the correlated evolution of the power spectrum. Propagating fluctuations through a hot flow which extends from and outer to inner radius, $r_o - r_i$, can produce the band limited noise characteristic of the continuum power spectrum, as well as producing the rms-flux relation (L97; K01; AU06). Lense Thirring precession of this *same* hot flow can produce the QPO, with frequency set by the *same* parameters of r_o and r_i , together with the surface density of the flow (IDF09). The surface density is itself given self consistently by mass conservation from the propagating fluctuations. This predicts that the surface density fluctuates, so predicts that the QPO frequency will vary on short timescales (i.e. that it is a quasi rather than true period). These fluctuations set an upper limit to the coherence of the QPO, and this increases (i.e. width decreases) as r_o decreases. This is due to the decrease in fluctuation power due to the smaller range of radii from which to pick up variability. All these features are well known properties of the data (e.g. Remillard & McClintock 2006; DGK07): this model gives the first quantitative description of their origin. The fluctuations also predict that the flux and QPO frequency are correlated on short timescales, as a perturbation in the surface density at large radii leads to a longer QPO frequency but has little effect on the luminosity. As this propagates down, it weights the mass distribution to smaller radii, increasing the QPO frequency but also increasingly contributing to the luminosity due to the centrally peaked emissivity. This behavior has also recently been observed (Heil et al 2011).

The model also gives a framework in which to interpret some otherwise very puzzling aspects of the energy dependence of the variability seen in BHB. The extended emission region can be inhomogeneous, with different parts of the flow producing a different spectrum. The outermost parts of the flow are closest to the cool disc, so will intercept more seed photons and have a softer spectrum than that produced in the more photon-starved inner part of the flow (Kawabata & Mineshige 2010; Makishima et al 2008; Takahashi et al 2008). This implies that a larger fraction of the lower energy Compton scattered photons come from larger radii in the flow than the higher energy ones. The higher frequency variability is preferentially produced at the smallest radii, where the spectrum is hardest. The flow at these small radii is also furthest from the cool disc, so has little reflection spectrum superimposed on the Compton continuum. Thus the model predicts that the fastest variability has the hardest spectrum and smallest reflected fraction, while slower variability has a softer spectrum and larger reflected fraction. This trend is also observed in the data (Revnivtsev et al 1999), and is very difficult to interpret in any other geometric picture as the inner disc edge cannot change in radius on even the longest timescale (few seconds) over which this relation is seen.

Similarly, the propagating fluctuations model means that a fluctuation starts at larger radii and then accretes down to smaller radii. Thus the fluctuation first affects the region producing a softer spectrum, then propagates down to smaller radii which produce the harder spectrum, so the hard band lags the soft band. The size of this lag depends on the frequency of fluctuations considered. Slow fluctuations (low frequencies) are produced at the outermost radius, so have the longest propagation time down to the innermost radius. High frequencies are produced only close to the inner radius, so only have a short distance to travel and hence have shorter lags. This gives rise to the frequency dependent time lags seen in the spectrum (Miyamoto & Kitamoto 1989; Revnivtsev et al 2001;

K01; AU06). In future work, we will quantitatively test these ideas against real data by incorporating a radial dependence of the emitted spectrum in our model, as well as putting in the more complex form for the radial dependence of the viscous frequency predicted from global ADAF models and use improved fit statistics (Ingram & Done, in preparation). We will also calculate the light curve shape predicted by Lense-Thirring precession of a hot inner flow, where the Comptonised emission is modulated by the difference in projected area of the (translucent) hot flow, self occultation and variation in seed photons from the different projected area of the disc (Ingram, Done & Zycki in prep). This predicts non-sinusoidal variability in the light curve i.e. this predicts the harmonic structure of the QPO.

While the many successes of the model are clearly evident, it is also clear that it is still far from complete. The most obvious outstanding issues are of the interaction of the hot flow with the truncated disc. The mechanism by which the cool disc truncates is not well established, though evaporation powered by thermal conduction between the two different temperature fluids almost certainly plays some role in this (Liu et al 1997; Rozanska & Czerny 2000; Mayer & Pringle 2007). Whatever the mechanism, it seems physically unlikely that this will give a smooth transition between a cool thin disc and the hot flow. Any inhomogeneities will probably also be amplified by the difference in velocity between the disc and flow (discs are close to Keplerian, while the hot flow is strongly sub Keplerian) so there will be a shearing turbulent layer formed between them. Recent results show that there is variability associated with the truncated disc at a few 10s of seconds in the low/hard state of the bright BHBs GX339-4 and SWIFT J1753.5-0127 (Wilkinson & Uttley 2009), suggesting that there is considerable complexity in the disc truncation (see also Chiang et al 2010). Full numerical simulations of the MRI in a composite truncated disc/hot inner flow geometry are probably required in order to show the effect of these. However, such simulations are way beyond current computer capabilities. A more tractable issue is the effect of relativity on the propagating fluctuations. Near the black hole, light bending and time dilation should be important and consequently future versions of this model need to take these effects into account. The final goal should of course be the creation of a fully relativistic model which can produce a Fourier resolved spectrum with both energy and time dependence such that we can test it against observations such as the PSD, the energy spectrum, the lag spectrum, the cross spectrum etc. This is of course very ambitious but it is the only way we can genuinely achieve a full theoretical understanding of what drives mass accretion and emission in BHBs.

10 ACKNOWLEDGEMENTS

AI acknowledges the support of an STFC studentship.

REFERENCES

- Agol E., Krolik J. H., 2000, ApJ, 528, 161
- Arévalo P., Uttley P., 2006, MNRAS, 367, 801
- Balbus S. A., Hawley J. F., 1998, RvMP, 70, 1
- Beckwith K., Hawley J. F., Krolik J. H., 2008, MNRAS, 390, 21
- Belloni T., Psaltis D., van der Klis M., 2002, ApJ, 572, 392
- Cabanac R. A., Valls-Gabaud D., Lidman C., 2008, MNRAS, 386, 2065
- Chiang C. Y., Done C., Still M., Godet O., 2010, MNRAS, 403, 1102
- Churazov E., Gilfanov M., Revnivtsev M., 2001, MNRAS, 321, 759
- Dexter J., Fragile P. C., 2011, ApJ, 730, 36

Done C., Gierliński M., Kubota A., 2007, *A&ARv*, 15, 1
 Fragile P. C., Mathews G. J., Wilson J. R., 2001, *ApJ*, 553, 955
 Fragile P. C., Blaes O. M., Anninos P., Salmonson J. D., 2007, *ApJ*, 668, 417
 Fragile P. C., 2009, *ApJ*, 706, L246
 Fragile P. C., Meier D. L., 2009, *ApJ*, 693, 771
 Frank J., King A., Raine D., 1992, *apa..book*,
 Gammie C. F., Popham R., 1998, *ApJ*, 498, 313
 Gierliński M., Done C., Page K., 2008, *MNRAS*, 388, 753
 Gierliński M., Nikotajuk M., Czerny B., 2008, *MNRAS*, 383, 741
 Gilfanov M., Revnivtsev M., Molkov S., 2003, *A&A*, 410, 217
 Gilfanov, M., & Arefiev, V. 2005, arXiv:astro-ph/0501215
 Heil L. M., Vaughan S., Uttley P., 2010, arXiv, arXiv:1011.6321
 Henisey K. B., Blaes O. M., Fragile P. C., Ferreira B. T., 2009, *ApJ*, 706, 705
 Ingram A., Done C., Fragile P. C., 2009, *MNRAS*, 397, L101
 Ingram A., Done C., 2010, *MNRAS*, 405, 2447
 Kawabata R., Mineshige S., 2010, *PASJ*, 62, 621
 Klein-Wolt M., van der Klis M., 2008, *ApJ*, 675, 1407
 Kotov O., Churazov E., Gilfanov M., 2001, *MNRAS*, 327, 799
 Krolik J. H., Hawley J. F., 2002, *ApJ*, 573, 754
 Lachowicz P., Done C., 2010, *A&A*, 515, A65
 Liu S., Melia F., 2002, *ApJ*, 573, L23
 Lyubarskii Y. E., 1997, *MNRAS*, 292, 679
 Liu B. F., Meyer F., Meyer-Hofmeister E., 1997, *A&A*, 328, 247
 Makishima K., et al., 2008, *PASJ*, 60, 585
 Markowitz A., et al., 2003, *ApJ*, 593, 96
 Mayer M., Pringle J. E., 2007, *MNRAS*, 376, 435
 Merloni A., Vietri M., Stella L., Bini D., 1999, *MNRAS*, 304, 155
 Misra R., Zdziarski A. A., 2008, *MNRAS*, 387, 915
 Miyamoto S., Kitamoto S., 1989, *Natur*, 342, 773
 Mueller, M., Madejski, G., Done, C., & Zycki, P. 2004, X-ray Timing 2003: Rossi and Beyond, 714, 190
 Mueller M., Madejski G., 2009, *ApJ*, 700, 243
 Narayan R., Yi I., 1995, *ApJ*, 452, 710
 Narayan R., Kato S., Honma F., 1997, *ApJ*, 476, 49
 Negoro H., Matsuoka M., Mihara T., Otani C., Wang T. G., Awaki H., 2000, *AdSpR*, 25, 481
 Noble S. C., Krolik J. H., 2009, *ApJ*, 703, 964
 Papadakis I. E., Lawrence A., 1993, *MNRAS*, 261, 612
 Psaltis D., Norman C., 2000, *astro*, arXiv:astro-ph/0001391
 Rao F., Belloni T., Stella L., Zhang S. N., Li T., 2010, *ApJ*, 714, 1065
 Remillard R. A., McClintock J. E., 2006, *AAS*, 38, 903
 Remillard R. A., Sobczak G. J., Muno M. P., McClintock J. E., 2002, *ApJ*, 564, 962
 Revnivtsev M., Gilfanov M., Churazov E., 1999, *A&A*, 347, L23
 Revnivtsev M., Gilfanov M., Churazov E., 2001, *A&A*, 380, 520
 Reynolds C. S., Miller M. C., 2009, *ApJ*, 692, 869
 Różańska A., Czerny B., 2000, *MNRAS*, 316, 473
 Schnittman J. D., 2005, *ApJ*, 621, 940
 Schnittman J. D., Homan J., Miller J. M., 2006, *ApJ*, 642, 420
 Shakura N. I., Sunyaev R. A., 1973, *A&A*, 24, 337
 Sobczak G. J., McClintock J. E., Remillard R. A., Cui W., Levine A. M., Morgan E. H., Orosz J. A., Bailyn C. D., 2000, *ApJ*, 544, 993
 Sobolewska M. A., Źycki P. T., 2006, *MNRAS*, 370, 405
 Stella L., Vietri M., 1998, *ApJ*, 492, L59
 Takahashi H., et al., 2008, *PASJ*, 60, 69
 Timmer J., Koenig M., 1995, *A&A*, 300, 707
 Titarchuk L., Osherovich V., 1999, *ApJ*, 518, L95
 Uttley P., McHardy I. M., 2001, *MNRAS*, 323, L26
 Uttley P., McHardy I. M., Papadakis I. E., 2002, *MNRAS*, 332, 231
 van der Klis M., 1989, *ARA&A*, 27, 517
 van der Klis M., 2004, *AdSpR*, 34, 2646
 Wagoner R. V., Silbergbeit A. S., Ortega-Rodríguez M., 2001, *ApJ*, 559, L25
 Wijnands R., van der Klis M., 1999, *ApJ*, 514, 939
 Wilkinson T., Uttley P., 2009, *MNRAS*, 397, 666
 Wilson C. D., Done C., 2001, *MNRAS*, 325, 167

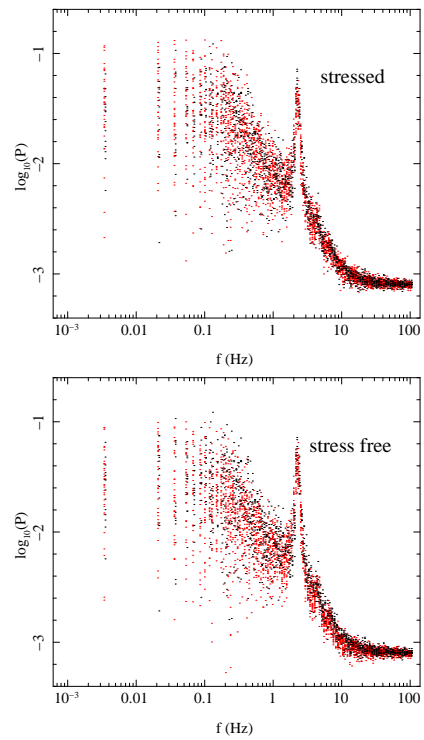


Figure A1. Raw periodogram points for both data (black) and model (red) with case 1 on the top and case 2 on the bottom (see text). As this is the data for observation 4, there are 14 black points per frequency bin. Our model calculates smoothed periodograms over 32 realisations so there are 32 red points per frequency bin.

APPENDIX A: A CLOSER LOOK AT THE STATISTICS

Here, we attempt to address some of the statistical problems encountered in section 7 by focusing in on observation 4 as it is a particularly striking example. The fit for the stressed version of the model (hereafter case 1) is plotted in the 4th panel from the top in Figure 10 and the fit for the stress free version (hereafter case 2) is plotted in the 4th panel from top in Figure 11. By eye, these fits both look excellent and are very difficult to tell apart. However, the rejection probability is 12% for case 1 and 72% for case 2! This is extremely confusing, especially considering that case 2 actually has a slightly lower χ^2 (23.0 compared to 23.8) than case 1! We will also discuss the obvious over fitting implied by such low χ^2 values later on in this section.

In an attempt to understand this discrepancy, we look a little closer at these two examples. It turns out that χ^2_{dis} for case 2 is larger than in case 1 (59207 for case 2; 53074 for case 1). Although this sheds a little light on the mystery, it doesn't explain such a huge discrepancy in rejection probability. However, the $\chi^2_{dis}(sim)$ values are all much smaller for case 2 meaning that the simulated values agree with each other much better than they do with the observed values, making it extremely unlikely that the observed points lie on the distribution of simulated points. In an attempt to see this difference, we plot all of the raw periodogram points for both cases in Figure A1. The black and red points are observed and simulated respectively with case 1 on the top and case 2 on the bottom. We see that the two plots are indistinguishable.

In Figure A2, we have looked at 3 specific frequencies: 0.1Hz (black), 9.5Hz (green) and 73Hz (blue) and created a histogram to see the distribution of periodogram values. Note, the three distri-

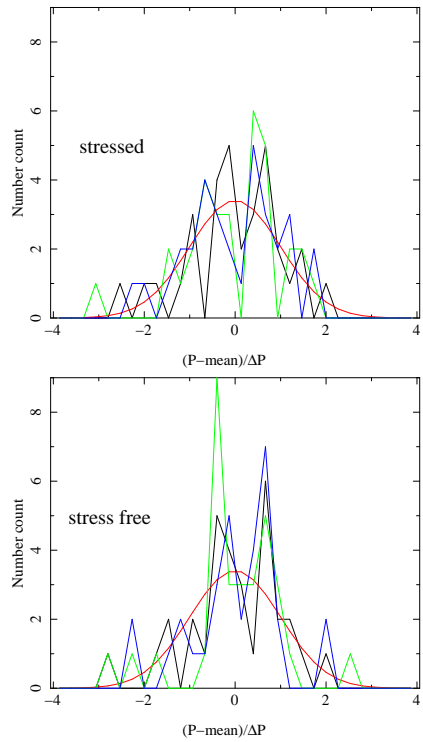


Figure A2. Histogram showing the distribution of periodogram points at $f = 0.1\text{Hz}$ (black), 9.5Hz (green) and 73Hz (blue) for case 1 (top) and case 2 (bottom). The three distributions have been normalised to have the same mean for clarity. We can see that these distributions have departures from a Gaussian (red line), especially in case 2.

butions have been normalised to have a mean of 0 and a standard deviation of 1 for clarity. Again, case 1 is on the top. Although there are departures from Gaussian behaviour in all of these distributions, it is clear that the distributions for case 2 are far more centrally peaked than those of case 1. This is consistent with $\chi^2_{dis}(sim)$ being smaller in general for case 2. There are also hints of baises which may account for the apparent over fitting implied by such small χ^2 values.

In our analysis, we calculated the logarithmically smoothed periodogram over $M = 32$ realisations in order to calculate and minimise χ^2 . We did this because Papadakis & Lawrence (1993) show that the logarithmically smoothed periodogram can have a Gaussian distribution if it is smoothed over more than $M = 20$ realisations, in comparision to the smoothed periodogram (i.e. no logarithms) where you would need more than $M = 50$ realisations. This implies that our logarithmically smoothed periodograms have a Gaussian error distribution, therefore making χ^2 an appropriate fit statistic. However, there are two problems with this, both arising because the error distribution depends on the underlying power spectrum. Papadakis & Lawrence (1993) were looking at red noise which is a significantly different variability process than that considered here. Therefore, just because 20 realisations are enough for them, doesn't mean it is enough for us. More significantly, the same authors show that the logarithmically smoothed periodogram may give a baised estimate of a power spectrum with a high curvature. Since, we are simulating QPOs, we are in this very regime which could explain the hint of bias displayed in Figure A2.

For these reasons, in a future paper (Ingram & Done in prep) we will use smoothed periodograms (no logarithms) and attempt to find a way around the resulting non-Gaussian errors. To do this,

we will consider statistical methods more general than χ^2 but less computationally intensive than minimising the rejection probability. Hopefully this will allow us to overcome these statistical problems.